

# Tidally generated internal-wave attractors between double ridges

P. ECHEVERRI<sup>1</sup>†, T. YOKOSHI<sup>1</sup>, N. J. BALMFORTH<sup>2</sup>  
AND T. PEACOCK<sup>1</sup>

<sup>1</sup>Department of Mechanical Engineering, Massachusetts Institute of Technology,  
Cambridge, MA 02139, USA

<sup>2</sup>Departments of Mathematics and Earth and Ocean Science, The University of British Columbia,  
Vancouver, BC V6T 1Z4, Canada

(Received 24 August 2009; revised 19 September 2010; accepted 23 September 2010;  
first published online 11 January 2011)

A study is presented of the generation of internal tides by barotropic tidal flow over topography in the shape of a double ridge. An iterative map is constructed to expedite the search for the closed ray paths that form wave attractors in this geometry. The map connects the positions along a ray path of consecutive reflections from the surface, which is double-valued owing to the presence of both left- and right-going waves, but which can be made into a genuine one-dimensional map using a checkerboarding algorithm. Calculations are then presented for the steady-state scattering of internal tides from the barotropic tide above the double ridges. The calculations exploit a Green function technique that distributes sources along the topography to generate the scattering, and discretizes in space to calculate the source density via a standard matrix inversion. When attractors are present, the numerical procedure appears to fail, displaying no convergence with the number of grid points used in the spatial discretizations, indicating a failure of the Green function solution. With the addition of dissipation into the problem, these difficulties are avoided, leading to convergent numerical solutions. The paper concludes with a comparison between theory and a laboratory experiment.

**Key words:** internal waves, stratified flows, topographic effects

---

## 1. Introduction

Internal tides are oceanic internal waves of tidal period that are generated as the barotropic (depth-independent) tide is forced to flow over topographic obstructions on the ocean floor. Examples of strong generation sites in the ocean include the Hawaiian island chain (Rudnick *et al.* 2003), the mid-Atlantic ridge (St Laurent & Garrett 2002), the Bay of Biscay (Pingree & New 1989) and the Luzon Strait (Jan, Lien & Ting 2008). The internal tides generated at such locations are believed to play an important role in ocean mixing, both near the generation site where breaking waves are reported, and in the far field where the radiated internal tide can interact with other waves and continental shelves (Garret & Kunze 2007).

Much recent theoretical effort has been directed at calculating the flux of energy scattered into internal tides for a range of idealized, two-dimensional topographic

† Email address for correspondence: paulae@alum.mit.edu

shapes and ambient physical conditions. The most popular and simple model is due to Bell (1975), who considered topography of infinitesimal height. Balmforth, Ierley & Young (2002) extended Bell's results to subcritical topography, for which the topographic slopes are everywhere less than the inclination of the scattered gravity waves. Llewellyn Smith & Young (2003), St Laurent *et al.* (2003) and Pétrélis, Llewellyn Smith & Young (2006) considered further extensions to isolated supercritical obstructions (for which the topographic slope exceeds the ray angles somewhere along the bottom) with the form of a 'knife-edge' or ridge in an ocean of finite depth. Nycander (2006) and Balmforth & Peacock (2009) considered periodic arrays of supercritical ridges in an infinitely deep ocean. Although these articles have painted a picture of internal tide generation, with the geometry adopted, the scattered internal waves always propagate away from the topography. In contrast, waves scattered from multiple ridges in a finite-depth ocean can become repeatedly reflected and trapped within the ridge system, converging to distinct geometrical structures known as wave attractors. To emphasize their origin and temporal frequencies, we refer to these tidally driven structures as 'internal tide attractors'.

Internal-wave attractors arise because gravity waves travel at angles determined by their intrinsic frequency and the local buoyancy and Coriolis frequencies. This leads to a curious reflection law at a boundary, so that multiple reflections in domains of nearly any shape can focus ray paths onto localized geometrical structures. These wave attractors have been demonstrated and studied in closed basins both theoretically and experimentally (Maas & Lam 1995; Maas *et al.* 1997; Grisouard, Staquet & Pairaud 2008; Hazewinkel *et al.* 2008).

The direct generation of wave attractors by tidal forcing has previously been investigated in astrophysical contexts and planetary science (Rieutord & Valdettaro 1997, 2010; Tilgner 1999; Ogilvie & Lin 2004). For the oceanic internal tide, double-ridge systems set the geometrical stage for attractors (Echeverri & Peacock 2010), demanding an extension of the existing tidal conversion calculations. Those calculations construct the time-periodic steady scattering state reached under prolonged tidal forcing, and compute the power radiated from the local spatial domain as a function of the tidal amplitude and frequency. However, when an attractor exists, a fraction of the scattered energy is continually focused onto the attractor within that domain, raising the possibility that dissipation may be required in order to yield a bounded solution (as for a resonantly forced normal mode). Indeed, inviscid solutions describing continual wave focussing into attractors display ever sharper spatial oscillations in the streamfunction as the attractor is approached, signifying an impending singularity in the velocity field (Wunsch 1969; Rieutord, Georgeot & Valdettaro 2001; Maas 2005). For continually forced inertial wave attractors in closed trapezoids, the addition of dissipation counters the geometrical focussing to lead to finite smooth solutions (Rieutord *et al.* 2001; Grisouard *et al.* 2008; Hazewinkel *et al.* 2008). A curious feature of those solutions is that the total energy dissipation approaches a constant value in the limit of vanishing dissipation that is independent of both the size of the dissipation and its mathematical form (Ogilvie 2005).

The goal of the current paper is to investigate internal tide conversion and attractors in two-dimensional double-ridge configurations. To help identify topographies that support internal tide attractors, we first derive a simple mapping method that can be used to locate closed ray paths. The map follows on from Maas & Lam (1995) and constructs the relation between the horizontal positions of consecutive reflections at the ocean surface following along each internal-wave ray. Such a mapping is inherently double-valued owing to the presence of rays propagating both left and right, and the

ambiguity must be removed by imposing additional rules. As a result, the construct is not a true one-dimensional map. Nevertheless, by reorganizing the pieces of the double-valued map on the squares of a checkerboard (Balmforth, Spiegel & Tresser 1995), the map can be rendered one-dimensional (an analogous construction is made by Rieutord *et al.* 2001). Although this procedure has limited advantage for finding wave attractors (as they can be computed from the double-valued map regardless), it does open up the possibility of using standard methods from dynamical systems theory to analyse the dynamics further.

To compute the internal tide scattered from the double ridges, we use the Green function approach outlined by Pétrélis *et al.* (2006). In part, the aim is to gauge how this method fares when internal tide attractors appear and the solution becomes more irregular. In fact, as we discover, the technique fails to give reliable results once there is an attractor. To remedy that situation, we incorporate dissipation into the computation using either a simple type of Rayleigh drag or a normal viscosity via a perturbative technique (which avoids the detailed imposition of the no-slip condition and allows us to continue to use a relatively simple Green function).

Further motivation for studying this type of topography comes directly from the ocean, and specifically the Luzon Strait, where internal tide dynamics in the vicinity of roughly two-dimensional double ridges has been recently observed (Zhao *et al.* 2004). With such applications in mind, and to make further contact with real fluid flows, we also compare the theory with a laboratory experiment. This experiment is designed along similar lines to the arrangements employed in two earlier, related studies (Peacock, Echeverri & Balmforth 2008; Echeverri *et al.* 2009), and uses particle-image velocimetry (PIV) to measure the wave fields shed from an obstacle towed back and forth inside salt-stratified water.

This paper is arranged as follows. In §2, we formulate the mathematical problem. Section 3 develops the one-dimensional map and the Green function formulation for internal tide generation is presented in §4. In §5, we present numerical results. Theoretical results are compared with a laboratory experiment in §6, and we conclude in §7.

## 2. Mathematical formulation

We begin with the Boussinesq equations for two-dimensional linear gravity waves described by pressure perturbation  $p(x, z, t)$  and velocity field  $(u(x, z, t), v(x, z, t), w(x, z, t))$ . The waves are generated by a background barotropic tidal flow of magnitude  $U_0$  and propagate in an ocean with constant Coriolis and buoyancy frequencies  $f$  and  $N$ . Including dissipation and denoting partial derivatives by subscripts, the governing equations are

$$\left. \begin{aligned} u_t - fv + \rho^{-1} p_x &= -v_j (-\nabla^2)^j u, \\ v_t + fu &= -v_j (-\nabla^2)^j v, \\ w_t + \rho^{-1} p_z - b &= -v_j (-\nabla^2)^j w, \\ u_x + w_z &= 0, \\ b_t + N^2 w &= 0, \end{aligned} \right\} \quad (2.1)$$

where  $\rho$  is a constant reference density, whereas fluctuations due to the waves are described by the buoyancy field  $b(x, z, t)$ . The terms involving the operator

$$D = v_j (-\nabla^2)^j \quad (2.2)$$

represent our models of dissipation, and reduce to a simple Rayleigh friction for  $j = 0$  and standard viscosity for  $j = 1$ . Rayleigh friction provides a model dissipation that does not change the mathematical structure of the boundary-value problem that we solve. Standard viscosity, on the other hand, is needed in order to compare theory with experiments, although the change to the boundary conditions required by the higher-order form of this term demands that we take a weakly dissipative limit in order to use the same solution technique.

We next assume that the tidally forced system approaches a time-periodic state with

$$(u, w) = \text{Re}[e^{-i\omega t}(-\phi_z, \phi_x)], \tag{2.3}$$

where  $\omega$  is the tidal forcing frequency and  $\phi(x, z)$  is the baroclinic streamfunction that must be added to the background barotropic component  $-U_0z$  to specify the full streamfunction. Elimination of all the variables in favour of  $\phi$  leads to

$$\left(1 + \frac{iD}{\omega}\right) \left[N^2 - \omega^2 \left(1 + \frac{iD}{\omega}\right)\right] \phi_{xx} = \left[\omega^2 \left(1 + \frac{iD}{\omega}\right)^2 - f^2\right] \phi_{zz}. \tag{2.4}$$

Ignoring free-surface displacements, no normal flow through the ocean surface,  $z = h_0$ , and bottom,  $z = h(x)$ , implies the boundary conditions

$$\phi(x, h_0) = 0, \quad \phi(x, h(x)) = U_0h(x). \tag{2.5}$$

We consider localized topography such that  $h(x) = 0$  for  $|x| > a$ , and so gravity waves are scattered outwards as the tide is forced to flow over that obstacle. If dissipation is included, the far-field conditions in  $x$  demand that  $\phi \rightarrow 0$  as  $|x| \rightarrow \infty$ ; if  $\nu_j \rightarrow 0$ , on the other hand, we employ an outgoing wave radiation condition. The inclusion of viscosity ( $j = 1$ ) should further require us to impose the full no-slip condition on the topography and a stress-free condition at the surface. We avoid these additional conditions here by treating the viscous term perturbatively, as alluded to above and described in more detail later.

Setting aside the viscous case for the moment, and considering only Rayleigh friction for which  $D$  is simply the constant factor  $\nu_0$ , we rewrite the internal-wave equation (2.4) in the form

$$\mu^2 \phi_{xx} = (1 + i\alpha)^2 \phi_{zz}, \tag{2.6}$$

which proves convenient for the analysis of §4, and contains two parameters  $\mu$  and  $\alpha$  representing wave slope and dissipation. These parameters are determined on separating the real and imaginary parts of the complex algebraic equation

$$\frac{(1 + i\alpha)^2}{\mu^2} = \frac{(\omega + iD)^2 - f^2}{N^2 - \omega(\omega + iD)}. \tag{2.7}$$

For example, when  $D$  is small compared to the characteristic frequencies  $\omega$ ,  $N$  and  $f$ ,

$$\mu \approx \sqrt{\frac{N^2 - \omega^2}{\omega^2 - f^2}} \quad \text{and} \quad \alpha \approx \frac{[N^2(\omega^2 + f^2) - 2\omega^2 f^2]D}{2\omega(\omega^2 - f^2)(N^2 - \omega^2)}. \tag{2.8}$$

Equations (2.5)–(2.6) can be made dimensionless by defining the variables

$$X = \frac{\pi x}{\mu h_0}, \quad Z = \frac{\pi z}{h_0}, \quad H(X) = \frac{\pi h(x)}{h_0}, \quad \varphi(X, Z) = \frac{\pi}{U_0 h_0} \phi(x, z). \tag{2.9}$$

The topography then has the dimensionless half-width  $A = \pi a / \mu h_0$  and height  $B = \pi \beta / h_0$ , where  $\beta$  is the maximum dimensional height of the topography, and

the dimensionless ocean depth is  $\pi$  wherever  $H \rightarrow 0$ . Moreover,

$$\varphi_{XX} = (1 + i\alpha)^2 \varphi_{ZZ}, \quad \varphi(X, H(X)) = H(X), \quad \varphi(X, \pi) = 0, \quad (2.10)$$

and  $\varphi(X, Z) \rightarrow 0$  or the outgoing wave condition as  $|X| \rightarrow \infty$ .

### 3. A one-dimensional checkerboard map

In the absence of dissipation, the dimensionless problem stated in (2.10) reduces to a standard wave equation. The characteristic curves are straight lines inclined at  $45^\circ$  in the  $(X, Z)$ -plane, corresponding to the ray paths of the internal tide (see, for example, the discussion in Maas & Lam 1995 concerning some practicalities in solving this equation). An internal tide attractor arises when these ray paths converge onto a closed orbit due to repeated reflections from the boundaries. Thus, the creation and destruction of internal tide attractors can be determined from geometry alone, and here we develop a one-dimensional (1D) map that proves to be a convenient tool in detecting their existence in double-ridge systems. The approach follows along lines similar to that of Maas & Lam (1995), although we extend the construction in order to generate a single-valued 1D map. In principle, this opens up the possibility of using standard tools from dynamical systems theory to study more completely the dynamics; here we use it mostly to provide a more transparent iteration scheme.

The mapping variable that we exploit is the horizontal position along the surface where a ray is reflected for the  $n$ th time, denoted by  $X_n$ . Unfortunately, a description using this variable alone is problematic as it cannot distinguish between leftward and rightward propagating waves. The ambiguity is illustrated in figure 1, which (in the inset to figure 1a) plots a sample ray path reflecting between the ocean surface and a double-cosine ridge with

$$H(X) = \begin{cases} B \left[ 1 - \cos\left(\frac{2\pi X}{A}\right) \right], & |X| \leq A, \\ 0, & |X| > A, \end{cases} \quad (3.1)$$

for the specific values of  $A = 1.6\pi$  and  $B = 1$ . (Note that this topography becomes supercritical for  $B > A/2\pi$ , which implicitly contains the actual ray slope  $\mu$  in view of our non-dimensionalization in (2.9).) The ray enters the ridge system from the left, and is subsequently reflected back and forth before exiting to the right. However, the path is exactly traversed in the opposite direction by a ray entering from the right. In other words, for each surface reflection, there are two possible subsequent reflections. Thus, the map  $X_{n+1} = f(X_n)$  that relates consecutive values of  $X_n$  is double-valued, as illustrated in figure 1(a). Note also that the map has a number of discontinuities which arise because supercritical topography casts shadows that abruptly appear and disappear as  $X$  varies.

To lift the double-valued degeneracy of the mapping points, we exploit the checkerboard construction of Balmforth *et al.* (1995). More specifically, we focus attention on the region  $-L < X < L$  containing the topography (i.e.  $A < L$ ), and ignore ray paths once they leave or before they intersect this region (since  $H = 0$ , such future or past itineraries are easily constructed). We then distinguish the reflection points of the two types of rays by defining the new coordinates  $Y_n = X_n + L$  or  $Y_n = X_n - L$  for the right-going and left-going rays, respectively, and employ the single-valued map  $Y_{n+1} = F(Y_n)$ . The reflection points of right-going rays are thereby positioned in the first and fourth quadrants of the larger square  $-2L < Y_n < 2L$  and the leftward rays are placed in the second and third quadrants. Right-going reflections that continue

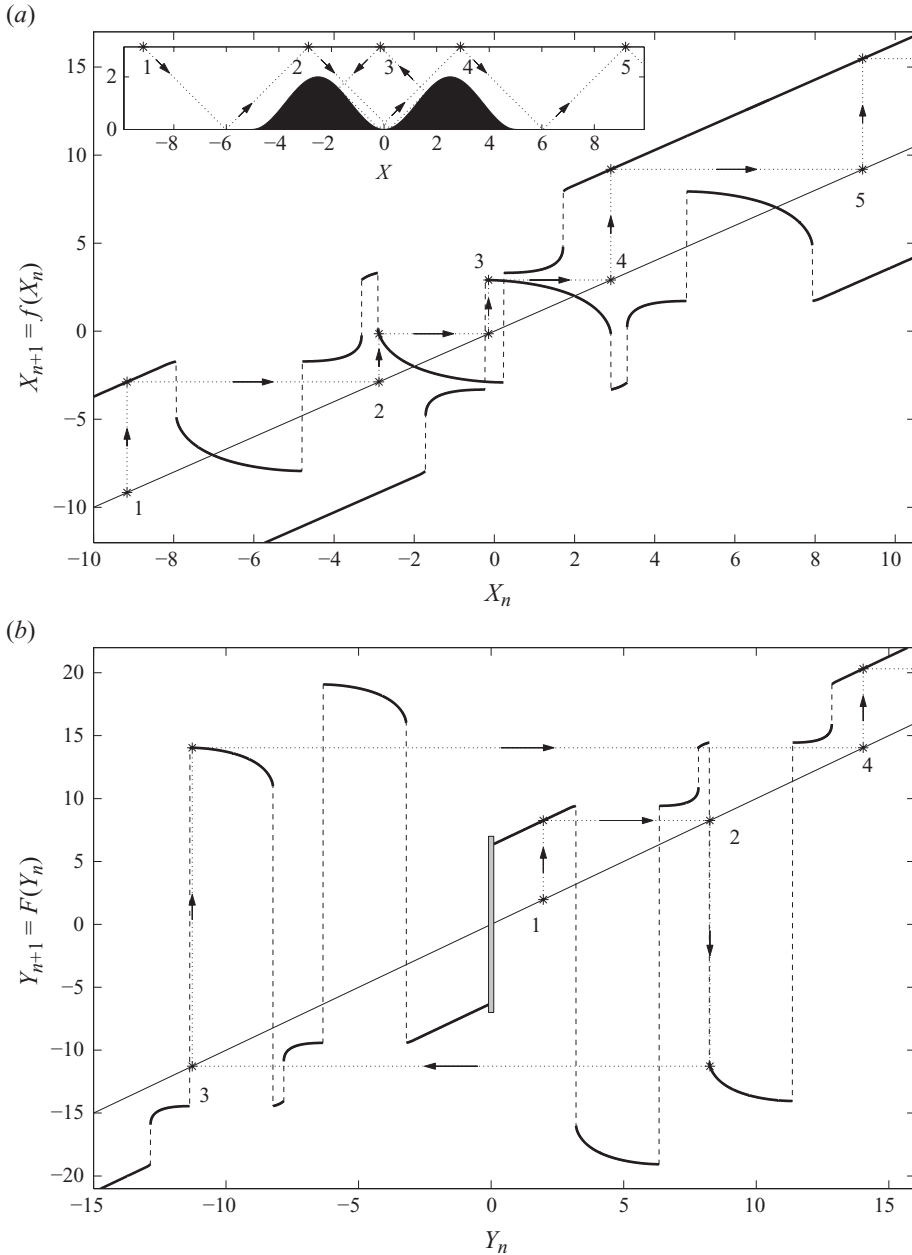


FIGURE 1. A sample ray path reflecting between the ocean surface and the topography (3.1) with  $A = 1.6\pi$  and  $B = 1$ . (a) The ray path (inset) and the corresponding orbit for the double-valued map that relates consecutive values of  $X_n$  (the surface reflection points, labelled by  $n$ ). (b) The checkerboard map that removes the double-valuedness of the map in (a); the shaded slender box at the origin indicates where rays incident from beyond the region of interest  $-L \leq X_n \leq L$  enter the map.  $L = 11$ .

to the right at the next reflection lead to sections of the map that are placed in the first quadrant, but if the subsequent reflection becomes left-going, the corresponding piece of the map is placed in the fourth quadrant, thereby accounting for the change in direction automatically. Similarly, left-going rays that continue left appear in the

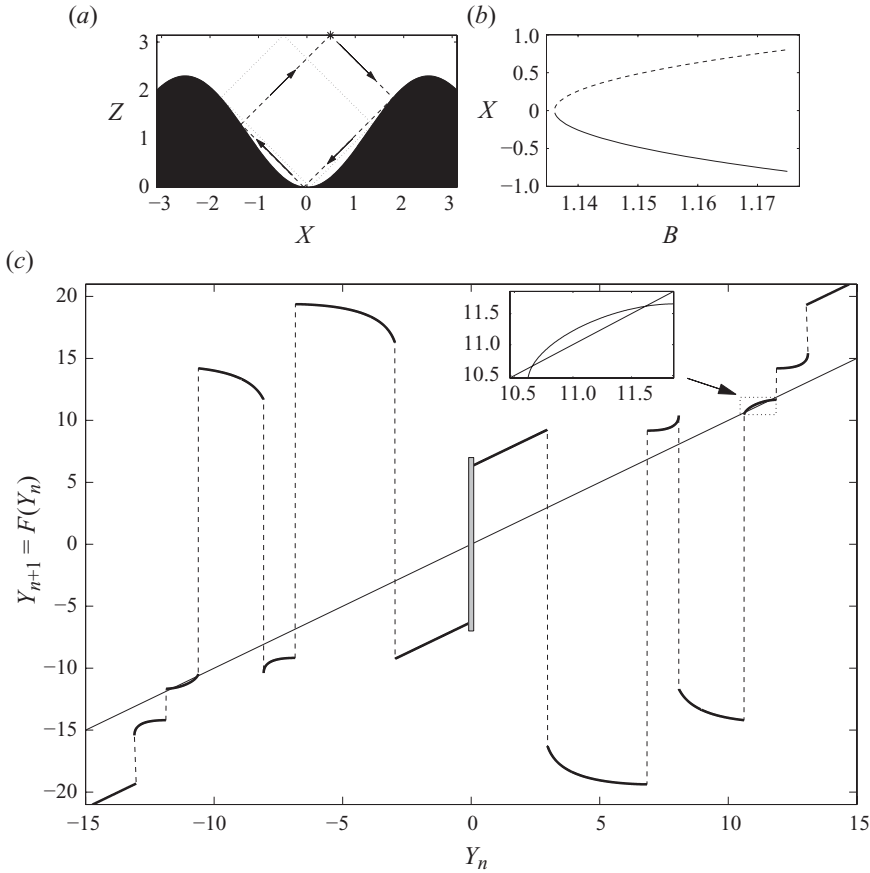


FIGURE 2. Closed orbits and checkerboard map for the double-cosine ridge (3.1). (a) The two closed ray paths with right-propagating surface reflections that exist at  $A = 1.6\pi$  and  $B = 1.15$ . The orbit that is stable is indicated by the arrows. Because of the symmetry of the topography, there are two identical orbits with rays propagating in the opposite direction (with left-going surface reflections), for which the sense of stability is interchanged. (b) A bifurcation diagram of the right-going surface reflection positions against  $B$ , with stable (unstable) orbits shown by solid (dashed) lines. (c) The checkerboard map corresponding to the orbit appearing in (a), with a magnification showing the structure near the two fixed points.

third quadrant, but left-going rays that are later reflected back to the right lie in the second quadrant. In other words, by placing the original sections of the double-valued map into appropriate squares of the checkerboard, we can automatically account for the transition rules between the right-going and left-going rays. Figure 1 illustrates the construction and the resulting removal of the degeneracy (taking  $L = 11$ ). Note that rays from outside the region of interest enter the map through the  $Y_{n+1}$ -axis, and we have placed a thin box over the relevant line to highlight this feature.

There are no closed orbits in the double-ridge configuration in figure 1. For  $A = 1.6\pi$  and  $B = 1.15$ , however, closed orbits exist, as illustrated in figure 2. The stability of these orbits, i.e. whether ray paths converge onto them, can be easily determined by computing the slope  $F'(Y_n)$  of the map  $Y_{n+1} = F(Y_n)$  at the corresponding fixed points (or at all the surface reflections if the attractor is geometrically more complicated). For right-going surface reflection (clockwise rays), one of the orbits in figure 2 is

stable, and therefore a wave attractor, whereas the other is unstable. Because the double ridges of (3.1) are symmetrical, there is a corresponding pair of closed orbits corresponding to left-going waves (anticlockwise rays), one of which is again an attractor, and which appear in the lower left corner of the map in figure 2(c). By varying  $B$  and tracking the orbits (see the bifurcation diagram in figure 2c), we find that the pairs appear in saddle-node bifurcations for smaller  $B$ , but disappear abruptly at higher  $B$  when the fixed points collide with discontinuities in the map (corresponding to the ray reflecting from a critical point on the topography). The saddle-node bifurcation point can be determined analytically by recognizing that the orbit must be reflected from the inner slopes of the topography at  $X = Z = \pi/2$ , implying  $B = \pi/[2(1 - \cos(\pi^2/A))]$ .

The internal tide attractors in figure 2 are the simplest types of closed orbits that can arise in a symmetrical double-ridge system. A multitude of more complex orbits involving multiple surface reflections appear in different regions of the  $(A, B)$ -parameter space via a rich bifurcation sequence. Moreover, if we desymmetrize the ridges, the orbit structures and their bifurcations are complicated still further. For the purpose of the current paper, we consider only the simplest types of attractors, as these are more robust and therefore more likely to be realized in either a laboratory experiment or a geophysical system such as the ocean.

#### 4. Internal tide generation

##### 4.1. Green function solution

By distributing an array of sources with density  $\gamma(x)$  along the topography, the streamfunction of the time-periodic problem (2.10) can be written down in terms of a Green function  $G(X, X', Z, Z')$  (cf. Pétrélis *et al.* 2006):

$$\varphi(X, Z) = \int_{-A}^A \gamma(X')G(X, X', Z, H(X')) dX'. \tag{4.1}$$

The Green function, constructed below, naturally incorporates the boundary conditions on the ocean surface ( $Z = \pi$ ) and in the far field ( $|X| \rightarrow \infty$ ). However, to enforce the boundary condition on the topography  $Z = H(X)$ , we must suitably choose the (currently unknown) source density, which leads to an integral equation for that function.

To calculate the Green function, we first note the equation it satisfies:

$$G_{XX} - (1 + i\alpha)^2 G_{ZZ} = i\delta(X - X')\delta(Z - Z'), \tag{4.2}$$

where  $\delta$  is the Dirac delta function. We consider the Fourier series representation (expansion in vertical modes, with  $p$  being the mode number):

$$G(X, X', Z, Z') = \sum_{p=1}^{\infty} G_p(X, X', Z') \sin pZ \tag{4.3}$$

and

$$G_p(X, X', Z') = \frac{2}{\pi} \int_0^\pi G(X, X', Z, Z') \sin pZ dZ. \tag{4.4}$$

Projecting the Green function equation onto  $\sin pZ$ :

$$\frac{\partial^2 G_p}{\partial X^2} + (1 + i\alpha)^2 p^2 G_p = \frac{2i}{\pi} \delta(X - X') \sin pZ', \tag{4.5}$$



which has the solution

$$G_p(X, X', Z') = \frac{\sin pZ'}{\pi p(1 + i\alpha)} e^{ip|X-X'|(1+i\alpha)}. \tag{4.6}$$

Thus,

$$G(X, X', Z, Z') = \sum_{p=1}^{\infty} \frac{\sin pZ \sin pZ'}{\pi p(1 + i\alpha)} e^{ip|X-X'|(1+i\alpha)}. \tag{4.7}$$

To satisfy the boundary condition  $\varphi(X, H) = H$ , the source density  $\gamma(X)$  must solve the integral equation

$$H(X) = \sum_{p=1}^{\infty} \frac{\sin pH}{\pi p(1 + i\alpha)} \int_{-A}^A \gamma(X') \sin pH' e^{ip|X-X'|(1+i\alpha)} dX', \tag{4.8}$$

where  $H = H(X)$  and  $H' = H(X')$ . Equations (4.1), (4.7) and (4.8) are the generalization of the inviscid theory presented by Pétrélis *et al.* (2006) and Balmforth & Peacock (2009) to incorporate the effects of Rayleigh friction. These articles also present formulae for the energy conversion rate, and we follow their example below. However, we take a different route in our derivation, attacking the wave equation and boundary conditions satisfied by  $\varphi(X, Z)$  directly, which allows us to incorporate friction and clarify its physical role.

#### 4.2. The conversion rate

Applying the operator  $\partial_X^2 - (1 + i\alpha)^2 \partial_Z^2$  to the definition of  $\varphi$  in (4.1) gives

$$\varphi_{XX} - (1 + i\alpha)^2 \varphi_{ZZ} = i\gamma(X)\delta(Z - H(X)). \tag{4.9}$$

Now

$$\varphi^* [\varphi_{XX} - (1 + i\alpha)^2 \varphi_{ZZ}] - \varphi [\varphi_{XX}^* - (1 - i\alpha)^2 \varphi_{ZZ}^*] = 2i\gamma_r(X)H(X)\delta(Z - H(X)), \tag{4.10}$$

where  $\gamma_r$  is the real part of  $\gamma$ , which can be rearranged into

$$\nabla \cdot \mathcal{J} = \frac{\partial \mathcal{J}_X}{\partial X} + \frac{\partial \mathcal{J}_Z}{\partial Z} = 2\gamma_r H \delta(Z - H) - \mathcal{D}, \tag{4.11}$$

where  $\mathcal{J} = (\mathcal{J}_X, \mathcal{J}_Z)$ , with

$$\mathcal{J}_X = i(\varphi\varphi_X^* - \varphi^*\varphi_X) \tag{4.12}$$

and

$$\mathcal{J}_Z = -i(\varphi\varphi_Z^* - \varphi^*\varphi_Z), \tag{4.13}$$

is equivalent to the dimensionless phase-averaged inviscid energy flux (cf. Balmforth *et al.* 2002), and

$$\mathcal{D} = 4\alpha|\varphi_Z|^2 + i\alpha^2(\varphi\varphi_Z^* - \varphi^*\varphi_Z)_Z - 2\alpha|\varphi|_{ZZ}^2 \tag{4.14}$$

is a dissipative term.

We now integrate (4.11) over the region above but not including the topography,  $-A \leq X \leq A$  and  $H(X) < Z \leq \pi$ , where the source term disappears. Then,

$$\int_{-A}^A \int_{H(X)^+}^{\pi} \nabla \cdot \mathcal{J} dZ dX = - \int_{-A}^A \int_{H(X)^+}^{\pi} \mathcal{D} dZ dX, \tag{4.15}$$

where  $Z = H(X)^+$  is to be interpreted as the limiting value from above. However, Gauss's Theorem indicates that the left-hand side of this expression is equal to

$$\int_0^\pi \mathcal{J}_X(A, Z) dZ - \int_0^\pi \mathcal{J}_X(-A, Z) dZ - \int_{-A}^A [\mathcal{J}_Z - H_X \mathcal{J}_X]_{Z=H^+} dX \equiv \mathcal{R} + \mathcal{L} - \mathcal{T}, \tag{4.16}$$

which contains the analogue of the right-going and left-going inviscid energy fluxes just beyond the topography,  $\mathcal{R}$  and  $\mathcal{L}$ , together with the analogue of the flux emanating from immediately above the topography itself,  $\mathcal{T}$ . The expression

$$\mathcal{T} - \mathcal{L} - \mathcal{R} = \int_{-A}^A \int_{H(X)}^\pi \mathcal{D} dZ dX \tag{4.17}$$

therefore corresponds to balancing the energy dissipation with the difference between the fluxes into and out of the region.

Instead of integrating over the region above the topography, we may also integrate over the domain  $-A \leq X \leq A$  and  $0 \leq Z \leq \pi$ . In this case, we pick up the contribution of the source, together with integrals over the region *below* the topography. In that region, the solution is simply  $\varphi = Z$  (satisfying the only two relevant conditions  $\varphi(X, 0) = 0$  and  $\varphi(X, H) = H$ ), and the corresponding integrals vanish leaving

$$\int_0^\pi \mathcal{J}_X(A, Z) dZ - \int_0^\pi \mathcal{J}_X(-A, Z) dZ \equiv \mathcal{R} + \mathcal{L} \tag{4.18}$$

$$= 2 \int_{-A}^A \gamma_r(X) H(X) dX - \int_{-A}^A \int_{H(X)}^\pi \mathcal{D} dZ dX. \tag{4.19}$$

Comparing the integral expression above with (4.16) provides the useful identity

$$\mathcal{T} \equiv \int_{-A}^A [\mathcal{J}_Z - H_X \mathcal{J}_X]_{Z=H^+} dX = 2 \int_{-A}^A \gamma_r(X) H(X) dX \tag{4.20}$$

(the derivation of the inviscid version of this relation by P  tr  lis *et al.* 2006 is more indirect and obscures its physical origin).

Alternative formulae for the leftward and rightward energy fluxes are provided by noting that

$$\varphi(X, Z) = \sum_{p=1}^\infty \frac{\gamma_p^\pm}{p(1 + i\alpha)} \sin pZ e^{\pm ipX(1+i\alpha)}, \tag{4.21}$$

with

$$\gamma_p^\pm = \frac{1}{\pi} \int_0^\pi \gamma(X') \sin pH(X') e^{\mp ipX'(1+i\alpha)} dX', \tag{4.22}$$

for  $X \geq A$  or  $X \leq -A$ , respectively. Hence,

$$\int_0^\pi \mathcal{J}_X(\pm A, Z) dZ \equiv \pm \sum_{p=1}^\infty \frac{\pi}{p} |\hat{\gamma}_p^\pm|^2, \tag{4.23}$$

where

$$\hat{\gamma}_p^\pm = \gamma_p^\pm e^{-\alpha p A} = \frac{1}{\pi} \int_0^\pi \gamma(X') \sin pH(X') e^{\mp ipX'} e^{-\alpha p(A \mp X')} dX'. \tag{4.24}$$

The Fourier series coefficients  $\gamma_p^\pm$  are weighted by the dissipative exponential factor  $\exp(-\alpha p(A \mp X'))$ , which can be interpreted as the spatial decay incurred as a wave launched at the position  $X'$  on the topography travels to  $X = \pm A$ .

Thus, we take  $\mathcal{T}$  to represent the total energy conversion from the barotropic tide and  $\mathcal{R} + \mathcal{L}$  to provide the total flux that reaches the edges of the topography and propagates beyond. The two differ by the energy dissipation that occurs within the fluid volume above the topography. If there are no waves that become confined within the bumps, then we expect that  $\mathcal{T}$  and  $\mathcal{L} + \mathcal{R}$  should be comparable in the limit of small dissipation. However, if there are attractors, the two fluxes may systematically disagree, as a fraction of the energy flux must be focused onto the attractor and dissipated there. Moreover, without dissipation, the focused energy cannot be removed, and the repercussions on the time-periodic problem are unclear.

Finally, we define the conversion rate to be

$$M = \frac{\mathcal{T}}{\pi B^2}, \quad (4.25)$$

which corresponds to the dimensionless energy flux using a slightly different scaling for the relevant vertical length (the topographic height, rather than the ocean depth; cf. Nycander 2006; Balmforth & Peacock 2009).

### 4.3. Viscous perturbation theory

For standard viscosity, we cannot proceed immediately down the path outlined above because  $D$  is a differential operator and formally one requires additional boundary conditions. Instead, as mentioned earlier, we take a perturbative approach that incorporates viscous effects purely as corrections to the inviscid model. The method follows along the lines outlined by Hurley & Keady (1997) in a related internal-wave problem, and was successful in allowing us to match theory with experiments in earlier tidal conversion problems (Peacock *et al.* 2008; Echeverri *et al.* 2009). In view of our intention to make further experimental comparisons, we ignore rotation and set  $f = 0$ .

The key idea is that when we look for solutions to the internal-wave equation in the form of a Fourier series in  $Z$ , the inviscid modes satisfy a second-order differential equation related to (4.5). With standard viscosity (and  $f = 0$ ), on the other hand, away from the topography that problem becomes fourth order:

$$\left(1 - \frac{i\omega D}{N^2 - \omega^2}\right) \frac{\partial^2 G}{\partial X^2} + \left(1 + \frac{iD}{\omega}\right) p^2 G_p = 0, \quad D \rightarrow \frac{\pi^2 v_1}{h_0^2} (\mu^{-2} \partial_X^2 - p^2), \quad (4.26)$$

where we have now fixed  $\mu = \sqrt{(N^2/\omega^2 - 1)}$ . Provided the kinematic viscosity  $v_1$  remains small, we may perturbatively calculate the weakly viscous, exponential solutions to (4.26) that decay as  $|X| \rightarrow \infty$  and which correspond to the inviscid solutions to (4.5). From these two solutions, we may build a Green function equivalent to (4.6), except that the constant  $\alpha$  is now replaced by the quantity  $\alpha_2 p^2$ , where

$$\alpha_2 = \frac{v_1}{2\omega} \left(\frac{\pi}{h_0}\right)^2 \left(\frac{N^2}{N^2 - \omega^2}\right)^2 \quad (4.27)$$

(cf. (2.8)). However, in constructing the Green function in this manner, we ignore the other pair of solutions to the fourth-order viscous problem. That pair can be interpreted as viscous boundary-layer solutions which are essential if one is to incorporate properly the full no-slip condition on the topography. Thus, by dropping those solutions and using the modified Green function, we effectively consider only the effects of viscous smoothing on the radiated inviscid wave field. Though non-rigorous, this does lead to a simpler solution technique that turns out to work well in comparison to experiments.

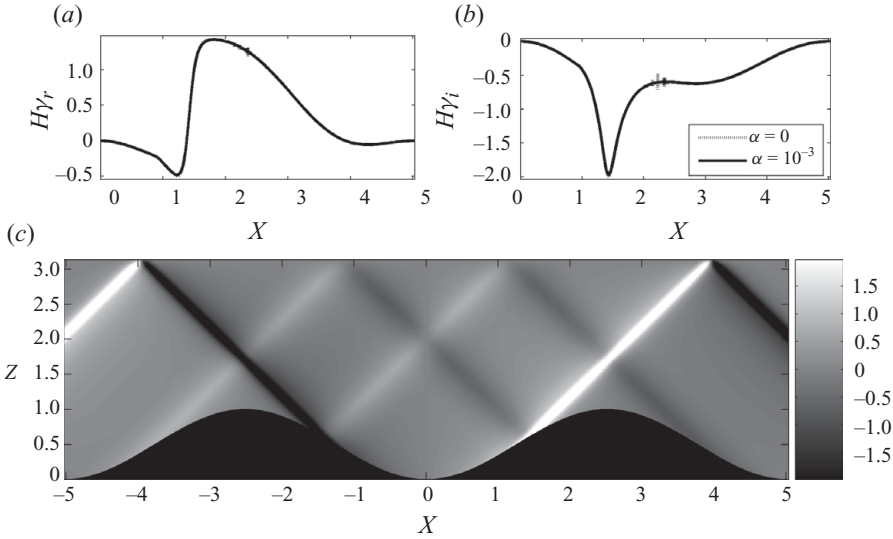


FIGURE 3. A subcritical solution for  $A = 1.6\pi$  and  $B = 0.5$ , with  $\alpha = 10^{-3}$  ( $K = P = 4000$ ). (a, b) The real and imaginary parts of the source density scaled by the topography (the inviscid results, with  $\alpha = 0$ , are also included as dotted lines for comparison). A snapshot of  $\phi_x$ , which is proportional to the buoyancy perturbation, is shown in (c).

In summary, to incorporate the effects of molecular viscosity, we use (4.7) and (4.8) with  $\alpha = \alpha_2 p^2$ . This allows us to build a Green function solution for the weakly viscous problem. With this solution in hand, we then compute the conversion rate  $M = \mathcal{F} / \pi B^2$  using (4.20), again in a perturbative sense.

## 5. Numerical results

### 5.1. Wave fields

The integral equation (4.8) for  $\gamma(X)$  is solved numerically by breaking the integration up into a uniform grid and applying the approximations described by Pétrélis *et al.* (2006) to evaluate each sub-integral, thereby turning the integral equation into an algebraic equation. We use a spatial grid containing  $K$  intervals and truncate the Fourier sum for the Green function at  $p = P$ ; practically, we take  $K = P = 1000$  or higher. With this numerical method, the inviscid boundary condition is satisfied exactly on the grid points and in between to the order of the accuracy of the quadrature rule (see Pétrélis *et al.* 2006 for further details). Results for the symmetrical double-cosine ridge system in (3.1) are used for illustration.

Three sample solutions are shown in figures 3–5. In the first example, presented in figure 3, the topography is subcritical and the wave field (shown in terms of the perturbed buoyancy field, which is proportional to  $\phi_x$ ) is dominated by waves scattered from the steepest parts of the topography (cf. Balmforth *et al.* 2002); a coincidence of the ray paths produces the strongest features. Note that we have plotted source densities  $\gamma(X) = \gamma_r(X) + i\gamma_i(X)$ , with an additional scaling of  $H(X)$ ; otherwise, sharp singular features dominate the source density at the locations where  $H \rightarrow 0$  (cf. Pétrélis *et al.* 2006, who actually use a source density  $\gamma(Z)$ , which also shows singular features where  $H'(X) \rightarrow 0$ ; both of these singularities do not appear to be detrimental to the numerical scheme).

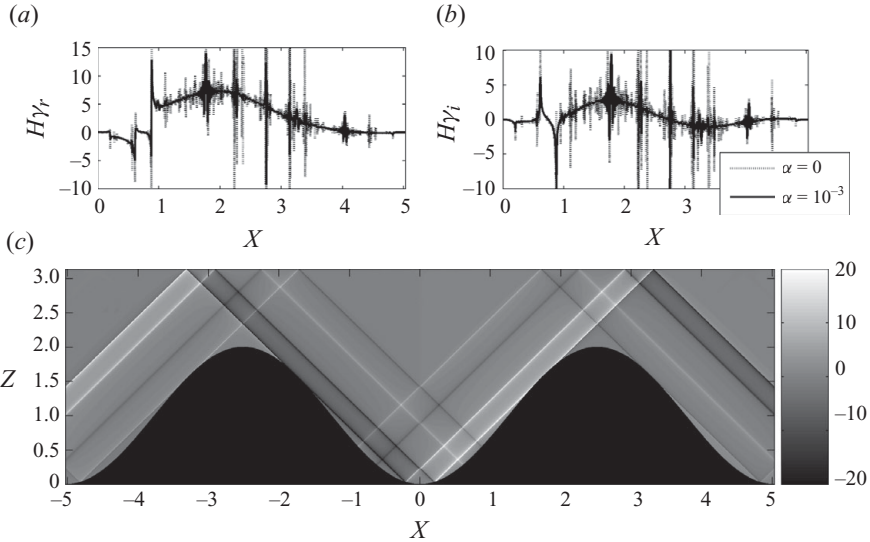


FIGURE 4. A supercritical solution for  $A = 1.6\pi$  and  $B = 1$ , with  $\alpha = 10^{-3}$  ( $K = P = 4000$ ). (a, b) The real and imaginary parts of the source density scaled by the topography (the inviscid results, with  $\alpha = 0$ , are also included as dotted lines for comparison). A snapshot of  $\phi_x$ , which is proportional to the buoyancy perturbation, is shown in (c).

A supercritical solution is presented in figure 4 and corresponds to the mapping example of figure 1. Sharp beams from points on the topography with critical slope now dominate the solution; without dissipation, the buoyancy field is formally singular along these beams (cf. Pétrélis *et al.* 2006; Balmforth & Peacock 2009). The source density also displays irregular sharp variations, which are smoothed by dissipation and which are partly connected to the reflections of the critical rays (but which also appear to be a by-product of the numerical scheme, see Pétrélis *et al.* 2006). Note that although the critical paths of the rays that dominate the wave field can be constructed geometrically, an appreciation of the full form of the wave field demands the Green function solution (in other words, the geometry of the characteristics alone does not sculpt the wave field).

Finally, figure 5 shows an example in which a pair of internal tide attractors exists between the double ridges, corresponding to the closed orbits shown in figure 2 (one created by clockwise travelling rays and the other by anticlockwise rays). The source density becomes dominated by peaks at the positions where the attractor reflects off the topography and the wave field is strongly focused on this geometrical object. There are no corresponding inviscid results presented for the source density in figure 5, because, as we show below, the Green function technique does not provide a reliable solution when there is an attractor.

## 5.2. Conversion rates

Having determined the source density, we use the integral  $M = \mathcal{F}/\pi B^2$  for evaluating the conversion rate and the Fourier sums  $\mathcal{L}/\pi B^2$  and  $\mathcal{R}/\pi B^2$  for the left–right fluxes. Figure 6(a) shows inviscid ( $\alpha = 0$ ) conversion rates above the double bumps for  $A = 1.6\pi$  and varying  $B$  (we vary the bump heights by changing  $B$  rather than their widths, by varying  $A$ , as the former leads to a simpler bifurcation sequence for the wave attractors). The conversion rate increases modestly with topographic amplitude for  $B < 1.135$ , with a sharper increase occurring when the topography

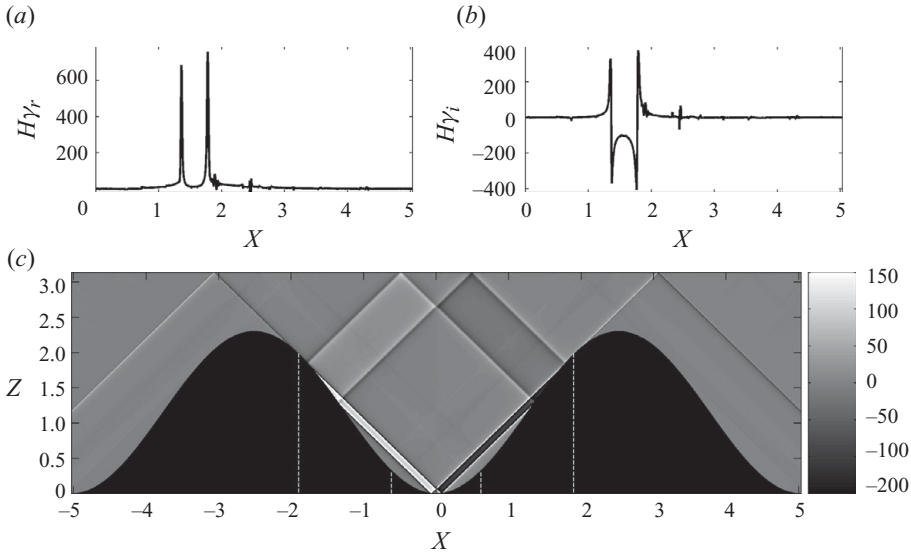


FIGURE 5. A supercritical solution for  $A = 1.6\pi$  and  $B = 1.15$ , with  $\alpha = 10^{-3}$  ( $K = P = 4000$ ); a pair of prominent attractors appears for this example, the left formed by anticlockwise travelling rays and the right by clockwise rays. (a, b) The real and imaginary parts of the source density scaled by the topography. A snapshot of  $\phi_x$ , which is proportional to the buoyancy perturbation, is shown in (c). The vertical dashed lines indicate the points with critical slope.

first becomes supercritical. More dramatic variations arise over the range  $\pi/2[1 + \cos(\pi^2/A)] < B < 1.176$ , which is shaded in the figure, over which a pair of attractors appears between the ridges (as illustrated in figures 2 and 5). For  $B > 1.176$ , the attractor disappears, leaving a conversion rate that initially declines, but finally oscillates due to a sequence of constructive and destructive interferences in the scattered wave field (cf. Balmforth & Peacock 2009). Except over the shaded range featuring the attractor, the conversion rate is relatively insensitive to the level of truncation,  $K = P$ , indicating that the solutions have largely converged with that level. In contrast, when the attractor appears, the numerical solutions display little sign of convergence as the truncation level is increased, offering numerical evidence that the Green function technique does not provide an inviscid solution (in line with the notion that energy constantly piles up towards the attractor, rendering the spatial structure of the time-periodic state more irregular).

Figures 6(b) and 6(c) show analogous results for our two models of dissipation. Even within the range of the attractor, the numerical solutions now converge with the truncation level ( $K = P$ ), indicating that dissipation counterbalances the energy pile-up on the attractor and regularizes the inviscid solution. Moreover, we observe a reliably substantial enhancement in the conversion rate (by an order of magnitude) at parameter settings close to where the attractor first appears.

The effect of varying the viscosity coefficient  $\alpha$  for Rayleigh friction is illustrated in figure 7. The sharpness and height of the peak in the conversion rate are influenced by the level of dissipation, although the different data collapse onto a common curve further from that peak. Overall, the computations suggest that if  $\alpha$  is taken sufficiently small, the conversion rate converges to a curve that is independent of the precise value of the viscosity or, indeed its form, as illustrated by the results for standard

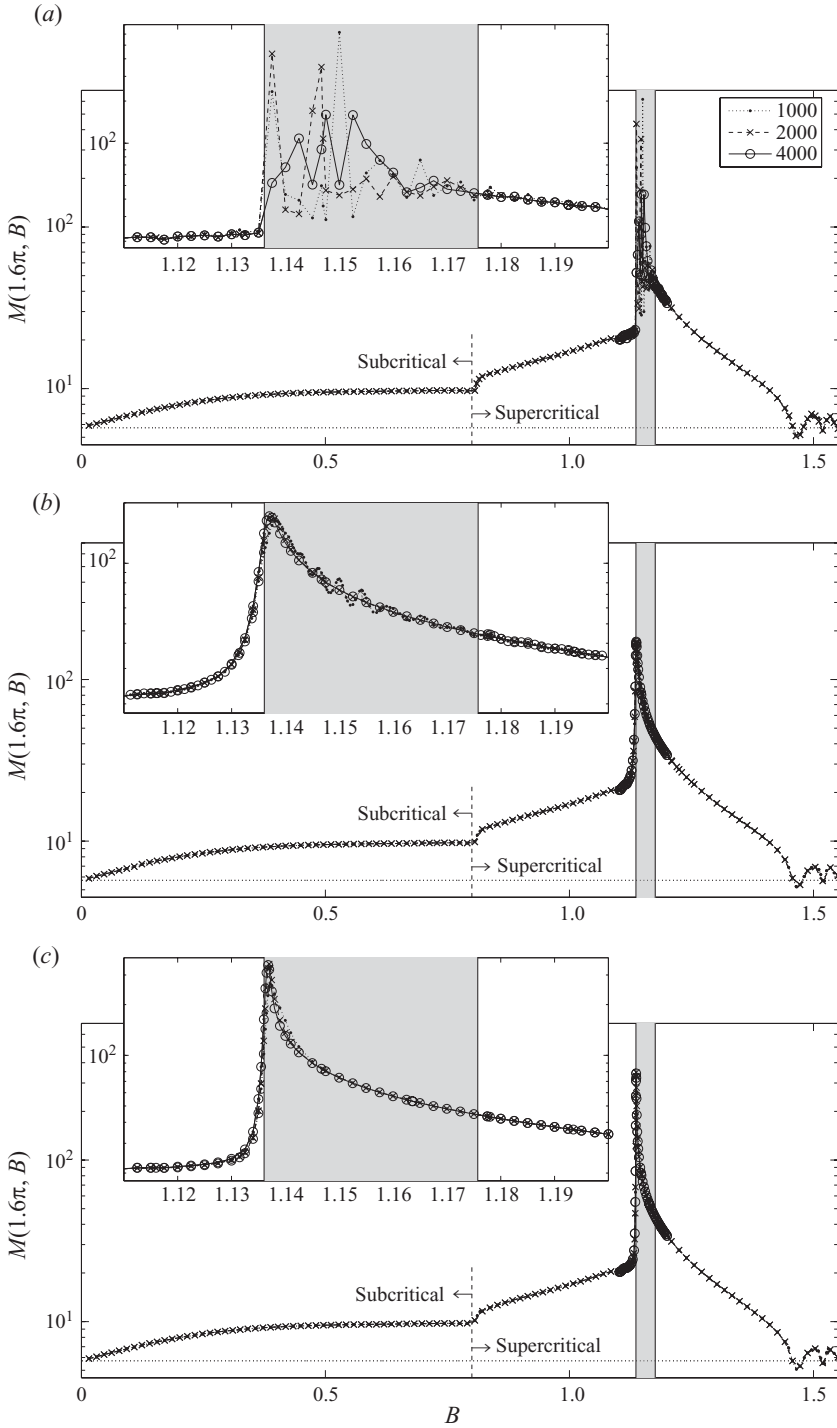


FIGURE 6. Conversion rates for  $A = 1.6\pi$  and varying  $B$  for (a)  $\alpha = 0$ , (b)  $\alpha = 10^{-3}$  and (c)  $\alpha = 10^{-7} p^2$ . In each case, three truncations are shown:  $K = N = 1000, 2000$  and  $4000$ . An attractor appears over the range of values for  $B$  that are shaded, and which is magnified in the insets. In the main panels, the horizontal dotted line illustrates Bell's result (infinitesimal topography), and the subcritical range is indicated.

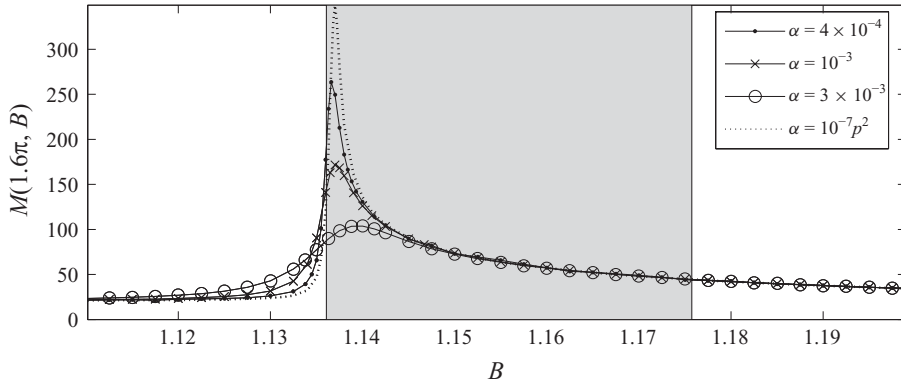


FIGURE 7. Conversion rates for  $A = 1.6\pi$  and varying  $B$ , with  $\alpha = 4 \times 10^{-4}$ ,  $10^{-3}$  and  $3 \times 10^{-3}$ . Also shown is the result for  $\alpha = 10^{-7} p^2$ .

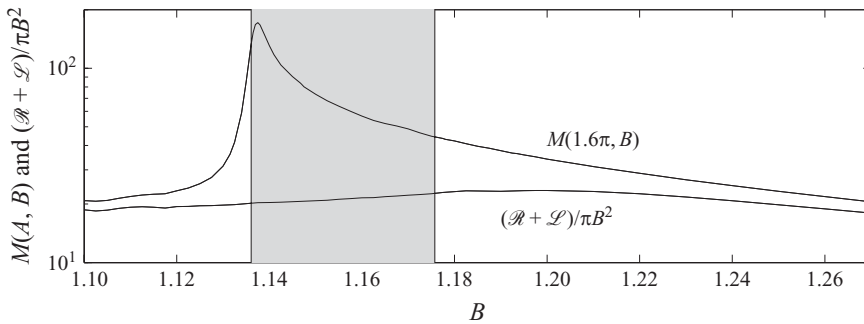


FIGURE 8. Conversion rates  $M(A, B) = \mathcal{F} / \pi B^2$  and the scaled left-right fluxes  $(\mathcal{R} + \mathcal{L}) / \pi B^2$  for computations with  $\alpha = 10^{-3}$ .  $A = 1.6\pi$ .

viscosity which are also included in figure 7 (except perhaps near the left border of the window containing the attractor, where that closed orbit appears in the saddle-node bifurcation). Although the convergence to a drag-independent conversion rate complements the asymptotic analysis by Ogilvie (2005), dissipation is essential to provide the smooth solution for  $\varphi(X, Z)$  that furnishes those conversion rates. It is also unclear whether the peak arising near the appearance of the attractor remains finite as  $\alpha \rightarrow 0$  and independent of the dissipation model.

Finally, figure 8 shows a comparison between  $M$  and the scaled outgoing flux  $(\mathcal{R} + \mathcal{L}) / \pi B^2$ . In contrast to the total conversion rate, the outgoing flux is a much smoother function of  $B$ , and although it is comparable to  $M(A, B)$  away from the window in which the attractor exists, there is a significant difference over that window, reflecting the dissipation on the attractor. Thus, we conclude that the appearance of the attractor coincides with a significant increase in energy conversion, with most of the energy focused onto that geometrical structure, as one might expect on qualitative grounds from solutions as those shown in figure 5. Although we have no quantitative explanation for the enhanced conversion, its origin may lie in the constructive interference of the wave patterns focussed onto the attractors, much like that found for tidal conversion from periodic arrays of supercritical ridges (Nycander 2006; Balmforth & Peacock 2009).



## 6. Experimental results

To test our theoretical prediction for internal tide attractors in double-ridge systems, we conducted a laboratory experiment using the apparatus described by Echeverri *et al.* (2009). In brief, an internal tide was generated in a rectangular tank filled with salt-stratified water by oscillating an obstacle immersed at the top of the tank back and forth at a prescribed (but adjustable) frequency. Instead of the double-cosine ridge, the obstacle was machine cut (to within 1 mm) into the shape of an asymmetrical pair of Gaussian ridges,

$$h(x) = h_1 \exp(-(x + x_0)^2/2\sigma^2) + h_2 \exp(-(x - x_0)^2/2\sigma^2), \quad (6.1)$$

with positions  $\pm x_0 = 0.151$  m, heights  $h_1 = 0.113$  m and  $h_2 = 0.225$  m and characteristic widths  $\sigma = 0.026$  m. The fluid depth was  $h_0 = 0.296 \pm 0.002$  m, the background stratification gave  $N = 1.01 \pm 0.01$  rad s<sup>-1</sup> and the kinematic viscosity was  $\nu = 1.07 \times 10^{-6}$  m<sup>2</sup> s<sup>-1</sup>. The oscillation amplitude was ramped up to a maximum value of 0.5 mm over several tidal periods and then left to run for sufficient time that a periodic state was achieved. PIV was used to visualize the wave field.

We select the profile (6.1), rather than our original double cosine in (3.1), because it permits one to tune the degree of asymmetry so that a single attractor is predicted to exist between the ridges (unlike symmetrical ridges which spawn pairs of attractors). The wave patterns are thereby expected to be simplified and more straightforward to visualize and compare with theory. The double-cosine ridge could also be desymmetrized in order to keep a similar algebraic form for the profile, but we have no reason to believe that the results would be different.

Figure 9 displays an attractor, together with the corresponding checkerboard map, for the experimental configuration. Also shown is a bifurcation diagram tracing the surface reflection points of closed orbits as the ray angle,  $\theta$ , is varied. Near  $\theta = 47.306^\circ$ , two pairs of closed orbits appear in a saddle-node bifurcation, corresponding to fixed points in the checkerboard map. As  $\theta$  is then lowered, one fixed point of each pair collides with a discontinuity in the 1D map and disappears (at  $\theta \approx 47.13^\circ$ ), leaving just two closed orbits. These comprise an attractor with a left-going surface reflection (and an anticlockwise ray path), as illustrated in figure 9(a), and an unstable orbit with a right-going surface reflection (and a clockwise ray path).

In figure 10, we present experimental results for three forcing frequencies corresponding to propagation angles of  $\theta = 29.4^\circ$ ,  $47.1^\circ$  and  $54.9^\circ$  (to within an error of  $\pm 0.2^\circ$ ). The results are snapshots of the magnitude of the vertical velocity in the three experiments, together with theoretical predictions using the viscous perturbation theory of §4.3. In all the cases, there is qualitative agreement between theory and experiment. Notably, for  $\theta = 47.1^\circ$  (figures 10b and 10e), where theory predicts the existence of an internal tide attractor, there is a dramatic increase in the strength of the internal tide between the ridges, with vertical velocities more than 15 times stronger than the forcing motion. The intensity of the structure between the ridges swamps all other features in the wave field, and near the ridge peaks the internal-wave activity was sufficiently strong that we were unable to record reliable PIV data.

A more quantitative comparison of experimental and theoretical results is presented in figure 11, which presents the envelope of the amplitude of the vertical velocity during the tidal cycle for vertical cross-sections at  $x = 0.05$  m. Theory compares tolerably well with the experiments for  $\theta = 29.4^\circ$  and  $54.9^\circ$ , the comparison being improved when the propagation angle used in the theory is adjusted (within the experimental uncertainty) to achieve the best fit with the experiments. For  $\theta = 47.1^\circ$ ,

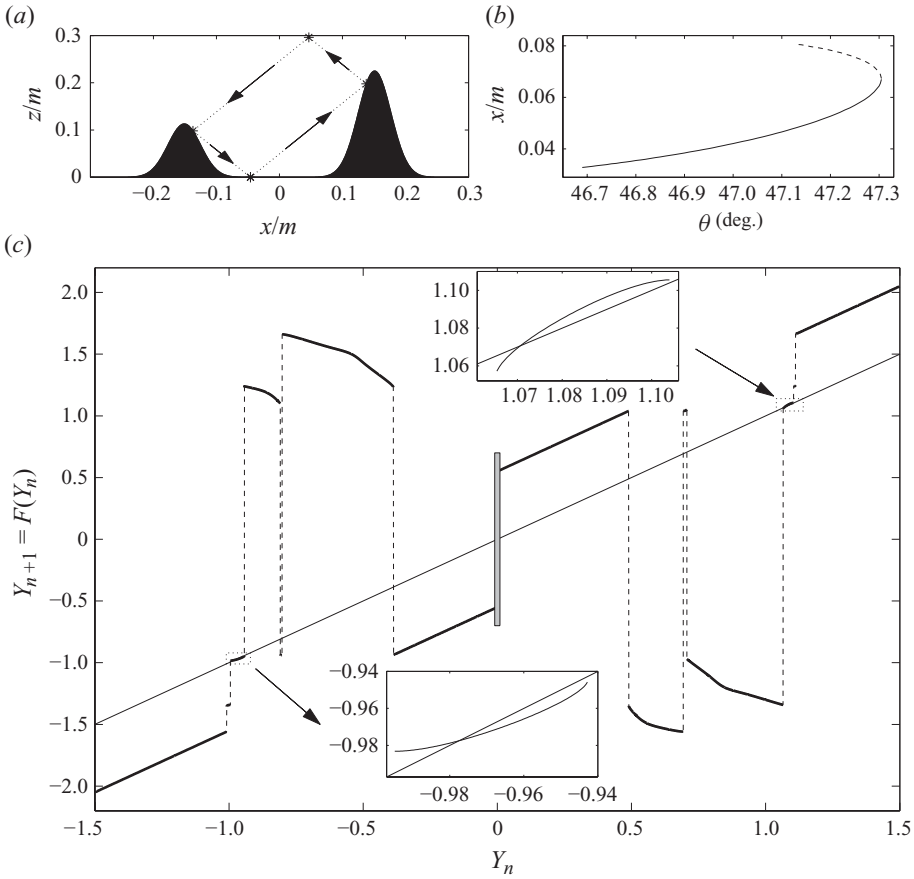


FIGURE 9. Attractors for the experimental configuration (6.1). (a) A stable closed orbit and (c) the corresponding checkerboard map, for an oscillation frequency adjusted so that internal waves propagate at an angle of  $\theta = 47.1^\circ$ . The checkerboard map is constructed using  $L = 1.024$  m, and the insets display details in the vicinity of the fixed points. (b) A bifurcation diagram for the closed orbits with left-going surface reflection points for varying ray angle  $\theta$  (corresponding to fixed points in the lower left part of the map in (c)). The two closed orbits appear in a saddle-node bifurcation at  $\theta \approx 47.306^\circ$ ; the solid line shows the attractor, for which rays propagate anticlockwise around the orbit; the dashed lines show the companion unstable orbit. There is a corresponding pair of closed orbits with right-going surface reflections (located in the upper right part of the checkerboard map), for which the sense of stability is switched. At  $\theta \approx 47.13^\circ$ , one orbit of each pair disappears (the stable orbit with a right-going surface reflection and the unstable orbit with the left-going surface reflection); the other two orbits disappear at  $\theta \approx 46.69^\circ$ .

when the attractor is present, the theory overpredicts the strength of the wave field by about a factor of two to three. Once again, however, there is a significant improvement when the propagation angle is adjusted. Indeed, we find that in the presence of an attractor, the wave field is highly sensitive to small variations in the system parameters.

Overall, the level of agreement between experiment and theory for the amplitude of the wave field in the presence of an attractor is remarkable given the perturbative fashion in which we have included viscosity, and that the wave field is assumed to be linear. There is, however, one notable discrepancy between theory and experiment. In the theory, there is a well-defined phase propagation corresponding

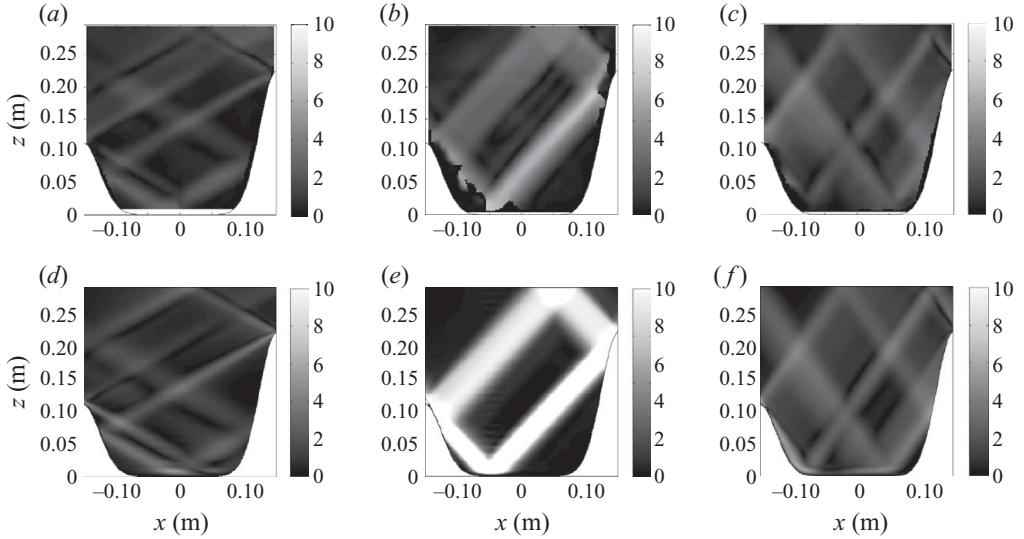


FIGURE 10. Experimental and theoretical snapshots of the vertical velocity magnitude between the ridges. (a–c) Experimental results for  $\theta = 29.4^\circ$ ,  $47.1^\circ$  and  $54.9^\circ$ , respectively, and (d–f) the corresponding viscous theoretical results. The attractor is present in (b) and (e). Velocity magnitudes are in  $\text{mm s}^{-1}$ .

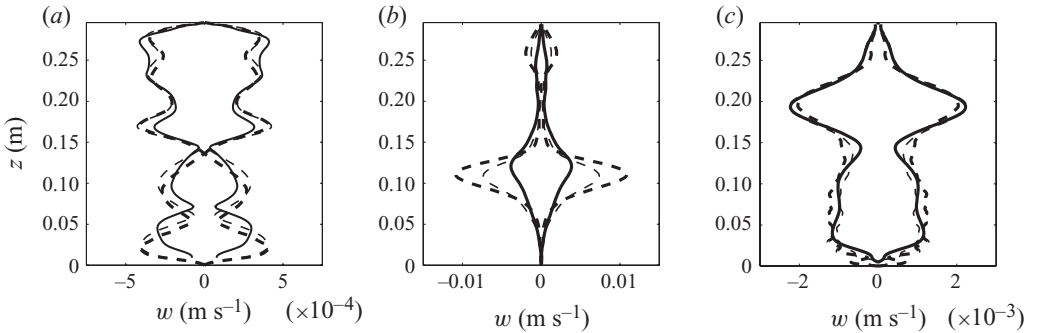


FIGURE 11. Comparisons of experimental (thick dashed lines) and theoretical vertical velocity profile envelopes (solid lines) at  $x = 0.05 \text{ m}$  for (a)  $\theta = 29.4^\circ$ , (b)  $47.1^\circ$  and (c)  $54.9^\circ$ . The thin dashed lines show theoretical results when the propagation angle is adjusted to achieve the best fit with the experiments.

to the anticlockwise energy flux for the attractor; for example, over the region in the lower right of figure 10(e) where signals are strong, the phase propagation is systematically downwards. On the other hand, the experimental signals display both upward and downward phase propagation over the same region. Similar discrepancies were reported by Lam & Maas (2008) for a parametrically forced attractor (Maas *et al.* 1997), and attributed to transient effects, with the theoretically expected phase propagation arising only over very long time scales in the experiments. Our experiments were run for similar durations of time, but we found no evidence for gradual adjustments in the phase propagation. Instead, the disagreement between theory and experiment may arise because the wave beams generated at the critical slopes of the topography lie very close to the relatively strong attractor, setting the stage for pronounced nonlinear wave interactions.

## 7. Conclusions

Through a combination of theory and experiment, we have demonstrated the existence of internal tide attractors in double-ridge systems. The attractor arises because of geometric focusing and trapping of the internal-wave rays by the topography. In order to predict the occurrence of attractors, it proved useful to develop a one-dimensional checkerboard map to identify closed ray paths and their stability as a function of the governing system parameters. In the presence of an attractor, the Green function technique for steady state, inviscid, internal tide generation apparently fails due to continual focussing of energy towards the attractor. We found that incorporating dissipation into the method regularizes the solutions in a manner that is independent of the magnitude and form of the damping, in agreement with a previous study (Ogilvie 2005). Furthermore, the weakly viscous solutions compare well with laboratory experiments.

This study differs from previous studies of internal-wave attractors (e.g. Maas *et al.* 1997) because the domain is open on both sides, allowing internal-wave rays to escape, and because the source of internal-wave energy comes from localized generation at sharp topographic features rather than from parametric forcing. In consequence, our results bear on the issue of whether internal-wave attractors are robust enough to exist in geophysical systems, where they are compromised by competing physical processes. A previous field study of the Mozambique Channel, for example, found no evidence of wave attractors (Manders, Maas & Gerkema 2004). While the chances for finding a geophysical attractor are potentially slim, the double-ridge configuration offers a promising scenario. An example is the Luzon Ridge, where studies using field data suggest the existence of attracting closed ray paths along a substantial northern portion of the ridge (Tang & Peacock 2010).

We acknowledge helpful discussions with Wenbo Tang and financial support through ONR grant N00014-09-0282. This work was partly conducted at the Geophysical Fluid Dynamics Summer Study Program at Woods Hole Oceanographic Institution.

## REFERENCES

- BALMFORTH, N. J., IERLEY, G. R. & YOUNG, W. R. 2002 Tidal conversion by subcritical topography. *J. Phys. Oceanogr.* **32**, 2900–2914.
- BALMFORTH, N. J. & PEACOCK, T. 2009 Tidal conversion by supercritical topography. *J. Phys. Oceanogr.* **39**, 1965–1974.
- BALMFORTH, N. J., SPIEGEL, E. A. & TRESSER, C. 1995 Checkerboard maps. *Chaos* **5** (1), 216–226.
- BELL, T. H. 1975 Lee waves in stratified flows with simple harmonic time dependence. *J. Fluid Mech.* **67**, 705–722.
- ECHEVERRI, P., FLYNN, M. R., WINTERS, K. B. & PEACOCK, T. 2009 Low-mode internal tide generation by topography: an experimental and numerical investigation. *J. Fluid Mech.* **636**, 91–108.
- ECHEVERRI, P. & PEACOCK, T. 2010 Internal tide generation by arbitrary two-dimensional topography. *J. Fluid Mech.* **659**, 247–266.
- GARRETT, C. & KUNZE, E. 2007 Internal tide generation in the deep ocean. *Annu. Rev. Fluid Mech.* **39**, 57–87.
- GRISOARD, N., STAQUET, C. & PAIRAUD, I. 2008 Numerical simulation of a two-dimensional internal wave attractor. *J. Fluid Mech.* **614**, 1–14.
- HAZEWINKEL, J., VAN BREEVOORT, P., DALZIEL, S. B. & MAAS, L. R. M. 2008 Observations on the wavenumber spectrum and evolution of an internal wave attractor. *J. Fluid Mech.* **598**, 373–382.

- HURLEY, D. G. & KEADY, G. 1997 The generation of internal waves by vibrating elliptic cylinders. Part 2. Approximate viscous solution. *J. Fluid Mech.* **351**, 119–138.
- JAN, S., LIEN, R. C. & TING, C. H. 2008 Numerical study of baroclinic tides in Luzon Strait. *J. Oceanogr.* **64**, 789–802.
- LAM, F. P. A. & MAAS, L. R. M. 2008 Internal wave focusing revisited; a reanalysis and new theoretical links. *Fluid Dyn. Res.* **40**, 95–122.
- LLEWELLYN SMITH, S. G. & YOUNG, W. R. 2003 Tidal conversion at a very steep ridge. *J. Fluid Mech.* **495**, 175–191.
- MAAS, L. R. M. 2005 Wave attractors – linear yet nonlinear. *Intl J. Bifurcation Chaos* **15**, 2757–2782.
- MAAS, L. R. M., BENIELLI, D., SOMMERIA, J. & LAM, F. P. A. 1997 Observation of an internal wave attractor in a confined stably-stratified fluid. *Nature* **388**, 557–561.
- MAAS, L. R. M. & LAM, F. P. A. 1995 Geometric focusing of internal waves. *J. Fluid Mech.* **300**, 1–41.
- MANDERS, A. M. M., MAAS, L. R. M. & GERKEMA, T. 2004 Observations of internal tides in the Mozambique Channel. *J. Geophys. Res.* **109**, C12034.
- NYCANDER, J. 2006 Tidal generation of internal waves from a periodic array of steep ridges. *J. Fluid Mech.* **567**, 415–432.
- OGILVIE, G. I. 2005 Wave attractors and the asymptotic dissipation rate of tidal disturbances. *J. Fluid Mech.* **543**, 19–44.
- OGILVIE, G. I. & LIN, D. N. C. 2004 Tidal dissipation in rotating giant planets. *Astrophys. J.* **610** (1), 477–509.
- PEACOCK, T., ECHEVERRI, P. & BALMFORTH, N. J. 2008 An experimental investigation of internal tide generation by two-dimensional topography. *J. Phys. Oceanogr.* **38**, 235–242.
- PÉTRÉLIS, F., LLEWELLYN SMITH, S. G. & YOUNG, W. R. 2006 Tidal conversion at a submarine ridge. *J. Phys. Oceanogr.* **36**, 1053–1071.
- PINGREE, R. D. & NEW, A. L. 1989 Downward propagation of internal tide energy into the Bay of Biscay. *Deep Sea Res. A* **36**, 735–758.
- RIEUTORD, M., GEORGEOT, B. & VALDETTARO, L. 2001 Inertial waves in a rotating spherical shell: attractors and asymptotic spectrum. *J. Fluid Mech.* **435**, 103–144.
- RIEUTORD, M. & VALDETTARO, L. 1997 Inertial waves in a rotating spherical shell. *J. Fluid Mech.* **341**, 77–99.
- RIEUTORD, M. & VALDETTARO, L. 2010 Viscous dissipation by tidally forced inertial modes in a rotating spherical shell. *J. Fluid Mech.* **643**, 363–394.
- RUDNICK, D. L., BOYD, T. J., BRAINARD, R. E., CARTER, G. S., EGBERT, G. D., GREGG, M. C., HOLLOWAY, P. E., KLYMAK, J. M., KUNZE, E., LEE, C. M., LEVINE, M. D., LUTHER, D. S., MARTIN, J. P., MERRIFIELD, M. A., MOUM, J. N., NASH, J. D., PINKEL, R., RAINVILLE, L. & SANFORD, T. B. 2003 From tides to mixing along the Hawaiian Ridge. *Science* **301**, 355–357.
- ST LAURENT, L. C. & GARRETT, C. 2002 The role of internal tides in mixing the deep ocean. *J. Phys. Oceanogr.* **32**, 2882–2899.
- ST LAURENT, L. C., STRINGER, S., GARRETT, C. & PERRAULT-JONCAS, D. 2003 The generation of internal tides at abrupt topography. *Deep Sea Res. I* **50**, 987–1003.
- TANG, W. & PEACOCK, T. 2010 Lagrangian coherent structures and internal wave attractors. *Chaos* **20**, 017508.
- TILGNER, A. 1999 Driven inertial oscillations in spherical shells. *Phys. Rev. E* **59**, 1789–1794.
- WUNSCH, C. 1969 Progressive internal waves on slopes. *J. Fluid Mech.* **35**, 131–141.
- ZHAO, Z., KLEMAS, V., ZHENG, Q. & YAN, X. H. 2004 Remote sensing evidence for baroclinic tide origin of internal solitary waves in the northeastern South China Sea. *Geophys. Res. Lett.* **31**, L06302.